Software-Defined Optoelectronics: Space and Frequency Diversity in Heterodyne Interferometry

Lucas M. Riobó, *Member, IEEE*, Francisco E. Veiras, *Member, IEEE*, María T. Garea, *Member, IEEE*, and Patricio A. Sorichetti, *Senior Member, IEEE*

***Abstract*— In this paper, a general architecture for the implementation of software-defined optoelectronic systems is described. This concept harnesses the flexibility of software-defined hardware to implement optoelectronic systems which can be configured to adapt to multiple high speed optical engineering applications. As an application example, a software-defined optical interferometer using a commercial software-defined radio platform is built. The system is tested by performing high speed optical detection of laser-induced photoacoustic signals in a concentrated dye solution. Using software modifications only, conventional single carrier and also multicarrier heterodyne techniques with space and frequency diversity are performed. The latter technique shows a noticeable performance improvement in single-shot interferometric measurements.**

***Index Terms*— Optoelectronic devices, interferometry, photoacoustic effects, open source hardware, software-defined hardware, signal processing algorithms.**

I. Introduction

In THIS work we propose a general architecture for the implementation of software-defined optoelectronic (SDO) systems. The SDO concept refers to optoelectronic systems in which most of the functionality associated with signal conditioning and processing is digitally implemented and controlled by software. This includes the optical signal modulation and demodulation, and coding and decoding, with minimum hardware modifications.

Most optoelectronic measuring systems require a stimulus (excitation signal) and process a response (received signal), and in a certain sense, the stimulus-response characterization method is related to the communication problem. In the latter, the receiver must estimate the unknown transmitted message through a noisy, dispersive and possibly time-varying channel. In the stimulus-response characterization problem, the channel characteristics must be estimated in real time through the comparison of the (known) transmitted and received signals. This concept is applied in many digital communication systems, where the transmission channel characteristics are estimated in real time to mitigate the effects of channel distortion, including the adaptation of the processing at the receiver (adaptive filtering) and the waveform at the transmitter (pre-distortion) [1], [2]. From this viewpoint, most optoelectronic measuring systems were designed with very little flexibility in the stimulus waveform. The SDO concept is particularly relevant for the design of optoelectronic measuring systems, since it lends naturally to the optimization of both the stimulus waveform and the signal processing of the response, in real time.

A crucial aspect of the SDO concept is the application of software-defined hardware (SDH). Nowadays, there are several SDH platforms that may be adapted to different requirements and applications [3]–[6], giving clear advantages in cost, versatility and performance. These flexible systems may be configured, even in real time, to adapt to various modulation and demodulation schemes, waveforms, bandwidths and modes of operation. In particular, software-defined radio (SDR) signal processing platforms are multi-functional, programmable and easy to upgrade [7]. SDR platforms are at present found in specific optoelectronic applications, such as photonic-based coherent radar systems [8], stabilization of optical frequency combs [9] and heterodyne detection in interferometry [10], [11].

As an application example of the SDO concept, we build a software-defined optical interferometer (SDOI) using a commercial SDR platform (LimeSDR, [12]). In this work, we apply the SDOI to the optical detection of laser induced photoacoustic (PA) signals. Our optical hardware setup consists of a balanced-path interferometer [13] in a Mach-Zehnder configuration. The interferometer arms are the output beams from an Acousto-Optic Modulator (AOM). They traverse a control volume and are combined by a single element interferometer [14]. The interferograms, in phase opposition, are detected by a balanced photodector. The system implementation takes advantage of the flexibility of SDR platforms to drive the AOM with complex modulation waveforms, and then digitally process the detected interferometric signals. This makes it possible to perform real-time phase demodulation in pulsed optical signals. Moreover, we switch between two SDOI operation modes by means of software modifications only. The first method consists in single-carrier heterodyne

Manuscript received April 25, 2018; accepted May 25, 2018. Date of publication May 30, 2018; date of current version June 26, 2018. This work was supported in part by four UBACYT grants from the Universidad de Buenos Aires under Grant 2014-2017 20020130100346BA, Grant 2017-2019 20020160100042BA, Grant 2016-2017 20020150200143BA, and Grant 2017-2019 20020160100052BA, and in part by ANPCyT under Grant PICT 2016-2204. The work of L. M. Riobó was supported by a doctoral scholarship from CONICET. The associate editor coordinating the review of this paper and approving it for publication was Dr. Marco Petrovich. *(Corresponding author: Lucas M. Riobó.)*

L. M. Riobó and F. E. Veiras are with GLOmAe, Departamento de Física, Facultad de Ingeniería, Universidad de Buenos Aires, Buenos Aires 1063, Argentina, and also with the National Scientific and Technical Research Council (CONICET), Buenos Aires 1425, Argentina.

M. T. Garea and P. A. Sorichetti are with GLOmAe, Departamento de Física, Facultad de Ingeniería, Universidad de Buenos Aires, Buenos Aires 1063, Argentina (e-mail: lriobo@conicet.gov.ar).

Digital Object Identifier 10.1109/JSEN.2018.2842143

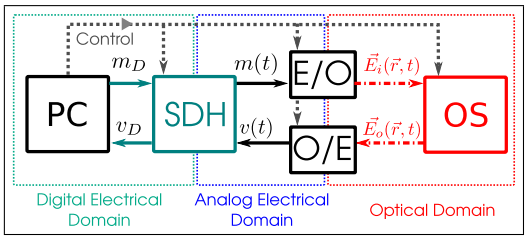

Fig. 1. A software-defined optoelectronic architecture. PC: Programmable controller, SDH: Software-defined hardware platform, $m(t)$: input electrical signal, $v(t)$ output electrical signal, E/O: Electrical-Optical block, O/E: Optical-Electrical block, $\vec{E}_i(\vec{r},t)$ input optical field(s), $\vec{E}_o(\vec{r},t)$ output optical field(s), OS: Optical System.

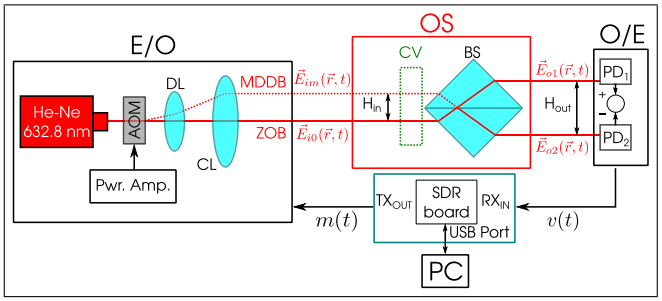

Fig. 2. Software Defined Optical Interferometer (SDOI) setup. AOM: Acousto-Optic Modulator, DL: diverging lens, ZOB: Zero Order Beam, MDDB: Modulation Dependent Diffracted Beam, CL: Converging Lens, H_{in}: separation between input beams, CV: Control Volume, BS: Beam Splitter, H_{out}: separation between output beams, PD: Photodiode. PC: Programmable Controller (Laptop computer).

detection, which is a basic technique to perform phase demodulation in heterodyne interferometry [15]. In the second method we drive the AOM with a multicarrier modulation signal. This modulation signal produces a set of spatially separated diffracted beams at the output of the AOM. When they combine in the balanced photodetector, after traversing the control volume, they produce an interferometric signal where the information is replicated on each carrier. We show that such space and frequency diversity improves single-shot interferometric measurements. Interestingly, a multicarrier modulation technique has been used in a synthetic array heterodyne detector [16]. Our setup is robust against environmental perturbations and the balanced photodetection provides high rejection to the intensity fluctuations of the laser source and stray incoherent light, which appear as common-mode signals [17], [18].

In section II, we describe the general SDO system architecture. As a specific application example of the SDO concept, in section III we describe in detail a SDOI. Then, we compare the performance of the two SDOI operation modes from the experimental results. We studied the PA signals produced by the pulsed laser irradiation of a concentrated fuchsin solution.

II. An Architecture for Software-Defined Optoelectronics (SDO)

An architecture for an SDO system is shown in Fig. 1. We consider three conceptual domains in the design of an optoelectronic system: optical, analog electrical and digital electrical. The optical domain is described in terms of fields, and the analog electrical domain in terms of analog signals. In the digital electrical domain, the description is given in terms of data streams. In this way, we can optimize the design at each domain, while preserving the operation flexibility of the system as a whole.

The constitutive elements of the domains are the functional blocks. The electrical-optical block (E/O) provides the optical setup (OS) with the input optical field(s) $\vec{E}_i(\vec{r},t)$ modulated by the input electrical signal $m(t)$. The output field(s) from the OS, $\vec{E}_o(\vec{r},t)$, is converted to the output electrical signal $v(t)$ by the opto-electrical block (O/E). The SDH platform provides the modulation signal $m(t)$ and processes $v(t)$. The programmable controller (PC) interfaces the SDH input and output data streams, m_D and v_D respectively, to the outside world. It also manages the SDH software components and provides any additional control signals. This topology forms a closed loop between the SDH and the OS. This has several advantages; for instance, it can provide self-synchronization between the transmitted and received signals. The SDH carries out the translation between the digital and analog domains. It can be used to implement many different waveforms for real-time system performance analysis. This enables the rapid prototyping, evaluation and testing of multiple optoelectronic systems at a lower cost. This configuration has two key advantages for the system designer: it reduces the computer processor workload at the PC and makes it possible to select the optimum SDH according to the different system requirements. Moreover, the PC and the SDH platform may be physically implemented as part of an embedded system.

In our SDO implementation example, a software-defined optical interferometer (SDOI), the PC is a laptop computer, the SDH is implemented with a software-defined radio (SDR) board and the optical system (OS) is a heterodyne interferometer. The implementation details are described in the next sections.

III. A Software Defined Optical Interferometer (SDOI)

In this section, we apply the concepts previously described in section II to the design of an SDOI. This interferometer is to be applied to the study of the optical properties of a sample inside a control volume. In Fig. 2 we show the main hardware components of each block of the SDOI.

A. Electrical-Optical Block (E/O)

A beam from a He-Ne laser source traverses an Acousto-Optic Modulator (AOM) which is driven by a wideband power amplifier excited by the modulation signal $m(t)$ from the SDR. The modulation signal produces a modulation-dependent diffracted beam (MDDB) within the AOM. The maximum diffraction efficiency is achieved by placing the AOM at the Bragg angle. The Zero Order Beam (ZOB) is unmodulated. The ZOB and the MDDB are collimated and separated by a backwards Galilean telescope (divergent lens, DL f=−25 mm, and convergent lens, CL f = 200 mm). In this way, the two parallel free beams $\vec{E}_{i0}(\vec{r},t)$ and $\vec{E}_{im}(\vec{r},t)$ enter the optical system (OS).

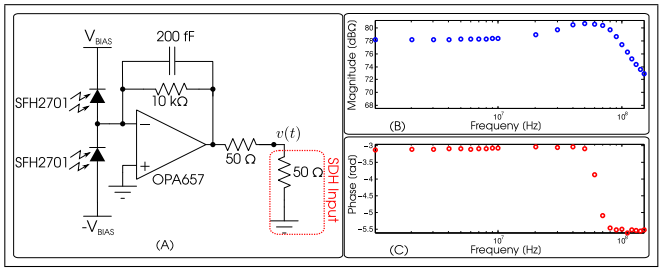

Fig. 3. (A) Balanced photodetector. Measured response: (B) Gain (dBΩ). (C) Phase.

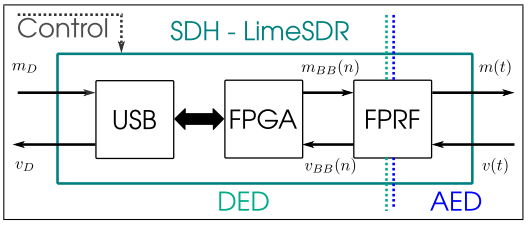

Fig. 4. Main functional blocks of the SDR. USB: Universal Serial Bus controller, FPGA: Field Programmable Gate Array, FPRF: Field Programmable Radio Frequency transceiver. DED: Digital Electrical Domain, AED: Analog Electrical Domain.

B. Optical System (OS)

The input free beams $\vec{E}_{i0}(\vec{r},t)$ and $\vec{E}_{im}(\vec{r},t)$ traverse the control volume, where their parameters (e.g. amplitude and phase) are modified by the optical properties of the sample under study. The beams $\vec{E}'_{i0}(\vec{r},t)$ and $\vec{E}'_{im}(\vec{r},t)$ at the output of the control volume, are recombined by a 50/50 ratio beam splitter (BS), as detailed in [14]. In this configuration, since the axes of the two parallel input beams are separated by a distance H_{in}, the output beams are also parallel, and separated by a distance H_{out} which is inversely proportional to H_{in}. The output beams $\vec{E}_{o1}(\vec{r},t)$ and $\vec{E}_{o2}(\vec{r},t)$ are given by

$$\vec{E}_{o1}(\vec{r},t) = \alpha_1\left[\vec{E}'_{i0}(\vec{r},t) + \vec{E}'_{im}(\vec{r},t)\right] \quad (1)$$

$$\vec{E}_{o2}(\vec{r},t) = \alpha_1\left[\vec{E}'_{i0}(\vec{r},t) - \vec{E}'_{im}(\vec{r},t)\right] \quad (2)$$

where α_1 describes the losses. Therefore, two interferograms $I_1(\vec{r},t)$ and $I_2(\vec{r},t)$ with a relative phase shift of π are produced,

$$I_1(\vec{r},t) \propto |\vec{E}_{o1}(\vec{r},t)|^2 = A(\vec{r},t) + B(\vec{r},t)\cos[\Delta\phi(\vec{r},t)] \quad (3)$$

$$I_2(\vec{r},t) \propto |\vec{E}_{o2}(\vec{r},t)|^2 = A(\vec{r},t) - B(\vec{r},t)\cos[\Delta\phi(\vec{r},t)] \quad (4)$$

where $A(\vec{r},t)$ is the background intensity, $B(\vec{r},t)$ is the fringe contrast and $\Delta\phi(\vec{r},t)$ is the phase difference between the beams $\vec{E}'_{i0}(\vec{r},t)$ and $\vec{E}'_{im}(\vec{r},t)$.

This compact, single-element design is symmetrical ("balanced-path interferometer"). This configuration has several advantages. First, undesirable effects arising from environmental perturbations and mechanical vibrations are attenuated. Also, the control volume may be modified, if desired, to be traversed by a single beam (either one of the two).

C. Optical-Electrical Block (O/E)

The O/E block receives the output beams $\vec{E}_{o1}(\vec{r},t)$ and $\vec{E}_{o2}(\vec{r},t)$ from the OS. Since PD_1 and PD_2 may be assumed to be identical square-law photodetectors, their outputs are proportional to the incident radiation intensities $I_1(\vec{r},t)$ and $I_2(\vec{r},t)$, Since the detection of the interferograms takes place on the photodiodes, located at fixed positions in space, in what follows it is unnecessary to indicate explicitly the dependence of I_1 and I_2 with $\vec{r}$. Therefore, the output signal $v(t)$ from the O/E may be written as the difference between the outputs of PD_1 and PD_2.

$$v(t) \propto I_1(t) - I_2(t) = 2B(t)\cos[\Delta\phi(t)] \quad (5)$$

In this SDOI, the photodetectors are reversed-bias photodiodes (SFH2701 [19]) used in a balanced configuration (Fig. 3). The output signal $v(t)$ is obtained from a wideband transimpedance amplifier (TIA) using a JFET input operational amplifier (Texas Instruments OPA657 [20]). The test procedure to characterize the response of the O/E is described in [11] and [21]. This front-end has a cut-off frequency (-3 dBΩ) of 120 MHz (Fig. 3(B)) and has a linear phase response up to 60 MHz (Fig. 3(C)). In the test results shown in Fig. 3, the output impedance of the E/O block (50 Ω) is matched to impedance of the load. In this implementation, the input impedance of the SDH is 50 Ω, according to the specifications of the SDR manufacturer.

The balanced detection at the O/E takes advantage of the symmetry between the output optical signals from the OS, allowing high common-mode rejection of the intensity fluctuations of the laser source and stray incoherent light. Consequently, the overall robustness of the system and the signal to noise ratio (SNR) of the output signal $v(t)$ are improved.

D. Software-Defined Hardware (SDH)

Since the optical properties of the sample in the OS control volume may modify both the amplitude and phase of the interferograms, in this SDOI it is convenient to use the phase and quadrature (I/Q) signal representation [1], [22] in the modulation and demodulation process. This allows us to use efficient and robust algorithms to synthesize the modulation signal $m(t)$ and to demodulate $v(t)$. Since most present-day SDR platforms are intended to be used in telecommunication systems with I/Q modulation formats, we chose a commercial SDR board (LimeSDR from LimeMicrosystems [5], [12]) to implement the SDH block. The main blocks of the SDR board are shown in Fig. 4.

The data streams m_D and v_D from the PC are exchanged between the PC and the SDH through an Universal Serial Bus (USB). At the SDR board, a Field Programmable Gate Array (FPGA) and a Field Programmable Radio Frequency (FPRF) transceiver synthesize the modulation signal $m(t)$ from a digital baseband signal $m_{BB}(n)$. They also demodulate $v(t)$ to a digital baseband signal $v_{BB}(n)$.

The modulation signal $m(t)$ is synthesized in the transmission side of the SDH block (Fig. 5(A)) from a digital complex signal $m_{BB}(n)$. It must be remembered that the MDDB at the E/O block is generated by the AOM from $m(t)$. In turn, $m(t)$ is chosen according to the desired functionality of the interferometer.

The specific characteristics of the real and imaginary components of $m_{BB}(n)$ are chosen according to the desired mod-

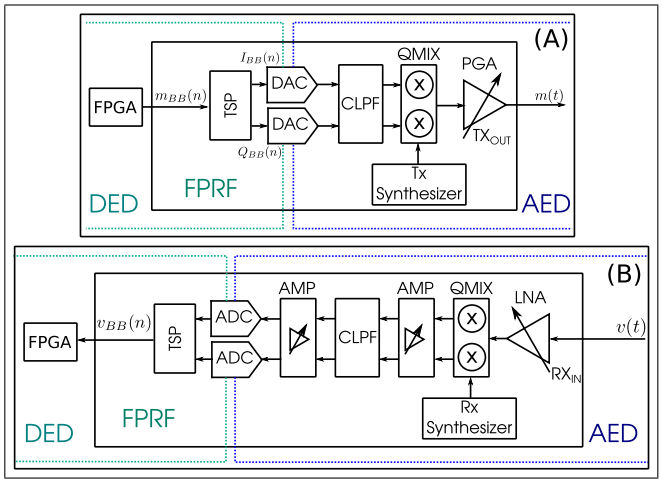

Fig. 5. (A) Transmission side of the SDH. TSP: SDR Built-in transceiver signal processor, DAC: digital to analog converter, QMIX: quadrature mixer, PGA: power gain amplifier. (B) Receiver side of the SDR. LNA: Low Noise amplifier, AMP: Amplifiers, ADC: Analog to digital converter. DED: Digital Electrical Domain, AED: Analog Electrical Domain.

ulation format and are defined by the software in the PC.

$$m_{BB}(n) = I_{BB}(n) + i\,Q_{BB}(n) \tag{6}$$

A built-in transceiver signal processor (TSP) in the SDR conditions and transmits the signal $m_{BB}(n)$ into the transmission path. Each one of the two components of $m_{BB}(n)$ is converted to an analog signal by a digital to analog converter (DAC), followed by a configurable low pass filter (CLPF). Then, a quadrature mixer (QMIX) performs the frequency upconversion to a defined carrier frequency ω_0. Finally, this passband signal is amplified by a power gain amplifier (PGA). Therefore, the modulation signal $m(t)$ may be written as,

$$m(t) = I_{BB}(t)\cos(\omega_0 t) + Q_{BB}(t)\sin(\omega_0 t) \tag{7}$$

The signal $v(t)$ at the output of the O/E block enters the receiver side of the SDR (Fig. 5(B) The signal $v(t)$ is amplified with a low noise amplifier (LNA) and a quadrature mixer performs the downconversion process of the signal. In this way, the in-phase and quadrature component of the signal are obtained. Then, two amplifiers (AMP) and a CLPF condition the signals before entering two analog-to-digital converters (ADCs). The ADCs deliver the components $v_I(n)$ and $v_Q(n)$ of the baseband digital complex signal $v_{BB}(n)$,

$$v_{BB}(n) = v_I(n) + i\,v_Q(n) \tag{8}$$

Finally, $v_{BB}(n)$ is pre-processed by the TSP, that generates the v_D data stream sent to the PC through the USB port.

E. Programmable Controller (PC)

In our implementation the PC block is a generic laptop computer. Taking advantage of the flexibility of the selected SDH, the PC is mainly dedicated to supervision and control tasks. It provides a friendly user interface, uploads the commands to the SDH, transmits and receives m_D and v_D data streams, and post-processes and displays the stored data. It is worth mentioning that the USB communication between the SDH and the PC may be replaced by a wireless link (e.g. Bluetooth).

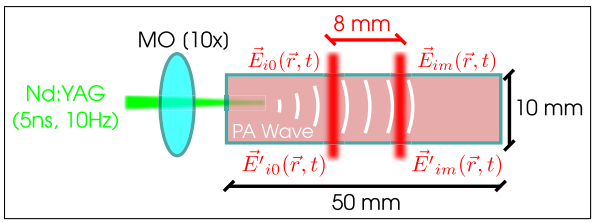

Fig. 6. Top view of the Control volume setup showing the interferometer beams inside the sample. MO: Microscope objective.

F. Software Environment

In the SDO architecture described in Sec.II, the software environment components reside at the PC and SDH blocks. The software components and tasks in each block may be flexibly chosen taking into account the hardware characteristics and the intended applications. In our SDOI implementation, the software components at the PC are the drivers and a user friendly graphical user interface (GUI) provided by the SDR manufacturer. This makes it possible to easily preconfigure the parameters of the SDR board (such as the gain of the amplifiers and cut-off frequencies of the CLPFs). In addition, the manufacturer also provides an application programming interface (API) for C and C++ software developers. We have also successfully tested programs using high-level software environments: GNU Radio [23], Octave and Python, to implement the software-defining behavior of the interferometer.

IV. Detection of Photoacoustic Signals Using SDOI

Photoacoustic signal generation is based on the excitation of ultrasonic waves by irradiating an object with short light pulses that have a duration in the range of picoseconds to nanoseconds. The mechanism responsible for the coupling of light into sound waves is the thermoelastic effect. Pulsed heating of light-absorbing structures causes a rapid temperature rise that results in an increase of pressure within the structures [24]. Relaxation of the overpressure after the pulse leads to the emission of ultrasonic waves that are measured outside the object and yield, via their arrival time and their temporal shape, information about location and size of the absorbers.

A Nd:YAG laser with a second harmonic generator (Continuum Minilite I, 532 nm, 5 ns, 10 Hz) focused by a microscope objective (MO, 10x) was used to generate a spherical pressure signal on a concentrated dye solution of Fuchsin (Basic Fuchsin, Standard Fluka) in distilled water. The sample was placed in an optical grade quartz cuvette (control volume), with dimensions 50 mm (Depth) × 50 mm (Length) × 10 mm (Width). The separation between the beams (H_{in}) is 8 mm, and the distance from the PA source is 5 mm. A schematic diagram of the control volume is shown in Fig. 6.

The photoacoustic wave produces a non-homogeneous, time-dependent refractive index variation $\Delta n(\mathbf{r}, t)$ in the propagating medium. This variation produces two main coupled effects on the beams of the interferometer. On the one hand, the inhomogeneity of the refractive index profile in the medium may change the amplitude of the received

signal. This effect is exploited in probe beam deflection techniques [25]. Moreover, the refractive index variation yields an optical path difference (OPD) between the beams that can be detected by interferometric methods [24], [26], [27]. Heterodyne interferometry techniques provide a way to decouple these effects. It must be noted that it is very difficult to provide such decoupling with homodyne interferometry, since both effects affect the amplitude of the interferogram. Also, to reach optimum sensitivity, the interferometric optical setups are usually stabilized, increasing the complexity of the experimental scheme. Frequently, a large number of pulses are averaged to improve the SNR of the measurement. In this work, the balanced-path design of the OS allows us to carry out a tabletop experiment over a home-made breadboard without passive or active stabilization, with satisfactory results in single-shot measurements.

The temporal resolution for the measurement of PA signals depends on the speed of sound in the media (approximately 1500 m/s), the cross section of the beams of the interferometer (3 mm^2) and the active area of the photodetectors (0.5 mm^2). Since the interferograms are detected directly over the photodiodes surface in the O/E block without focusing, the ratio between the speed of sound and the area of one photodiode gives a temporal resolution of about 0.4 μs (i.e a bandwidth of about 2 MHz) [24]. Fig. 6 shows that both beams will sense the PA wave in two different regions in the sample. The information from the photoacoustic signal is recovered from the phase difference $\Delta\phi(t)$ between the beams $\vec{E}'_{i0}(\vec{r},t)$ and $\vec{E}'_{im}(\vec{r},t)$, at the output of the control volume. This phase difference depends on the integrated effects of the refractive index variations along the propagation paths in the control volume, $n_{i0}(t)$ and $n_{im}(t)$ [24]. Therefore,

$$\Delta\phi(t) = \frac{2\pi}{\lambda} L\,[n_{i0}(t) - n_{im}(t)] \tag{9}$$

where L is the length of the propagation path within the sample in the control volume. In our experiment, we assume that the sample is acoustically non-dispersive in the frequency range of interest. Thus, the integrated refractive index variation for each beam are related as,

$$n_{im}(t) = \alpha_2\, n_{i0}(t - \Delta t) \tag{10}$$

where α_2 is an attenuation constant and Δt is a time delay that depends on the geometric distance between the beams and the speed of sound in the medium. Consequently, two proportional and time delayed responses with opposite signs are produced within the interferograms. In Eq. (10), it is assumed that the PA wave reaches the $\vec{E}_{i0}(\vec{r},t)$ (unmodulated) beam first, as it is clear from Fig. 6. It must be stressed that if the PA wave reaches the modulated $\vec{E}_{im}(\vec{r},t)$ first, for instance by switching the relative position of both beams, Eq. (9) is unchanged but $n_{im}(t)$ and $n_{i0}(t)$ switch places in Eq. (10).

The flexibility of the SDOI makes it possible to use different modulation and demodulation techniques to improve the recovery of the phase information while at the same time rejecting the amplitude variations. This is particularly important in single-shot measurements. In the following sections we present the results using conventional (single carrier) and multicarrier heterodyne interferometry.

A. Single-Carrier Heterodyne Interferometry

In this technique, the modulation signal $m(t)$ is a single carrier at an angular frequency ω_0 which excites the E/O block. To synthesize $m(t)$, both components of the complex signal of Eq. (6) must be constant. For instance, setting $I_{BB}(n) = A$ and $Q_{BB}(n) = 0$, from Eq. (7) we obtain,

$$m(t) = A\cos(\omega_0 t) \tag{11}$$

where A is the amplitude of the driving signal and ω_0 is the carrier frequency. Therefore, the MDDB at the output of the E/O block is a single first-order diffracted beam $\vec{E}_{i1}(\vec{r},t)$, whose intensity depends on A and its frequency is shifted from $\vec{E}_{i0}(\vec{r},t)$ by ω_0. After traversing the OS, the interfering beams, $\vec{E}_{o1}(\vec{r},t)$ and $\vec{E}_{o2}(\vec{r},t)$, are detected by the O/E block, which provides the output signal $v(t)$ to the SDH. Therefore, the signal at the SDR receiver is, (Eq. (5))

$$v(t) \propto 2B(t)\cos[\omega_0 t + \Delta\phi(t)] \tag{12}$$

The demodulation scheme is configured as a direct quadrature conversion receiver [1], [22] by setting the receiver synthesizer at ω_0. Therefore, the components of the output complex baseband digital signal ($v_{BB}(n)$ Eq. (8)) from the receiver are

$$v_{BB}(n) \propto B(n)\{\cos[\Delta\phi(n)] + i\,\sin[\Delta\phi(n)]\} \tag{13}$$

where the digitized instantaneous phase difference is retrieved by computing,

$$\Delta\phi(n) = \arctan\left[\frac{Im\{v_Q(n)\}}{Re\{v_I(n)\}}\right] \tag{14}$$

In this implementation, a single carrier signal at $\omega_0 = 2\pi$ 70 MHz drives the AOM. Once the interferograms are detected, the signal $v(t)$ is downconverted into baseband as described in Sec. III-F. Then, the downconverted signal is filtered by the CPLF with a cut-off frequency that matches the sensor, i.e. 2 MHz. Finally, the signal is digitalized at 40 Msps and $\Delta\phi(n)$ is recovered by the PC from the v_D data stream (Eq. 14). The functional blocks of the experimental scheme using single carrier heterodyne interferometry are shown in Fig. 7(A). In Fig. 7(B) we show the measured instantaneous phase difference between the two beams $\vec{E}'_{i0}(\vec{r},t)$ and $\vec{E}'_{i1}(\vec{r},t)$, Eq. (9), originated by a single PA wave generated by an optical pulse of 500 μJ on a sample containing a 100 μM solution of fuchsin in water.

In the next section, we describe the multicarrier heterodyne technique that improves the single-shot measurement SNR by using space and frequency diversity.

B. Multicarrier Heterodyne Interferometry

To implement this technique, we exploit the flexibility of the SDR system to produce a multicarrier (frequency comb) signal. From Eq. (6) $m_{BB}(n)$,

$$m_{BB}(n) = \sum_{n=1}^{N} I_{BB}\cos(\omega_n n) + i\,Q_{BB}\sin(\omega_n n) \tag{15}$$

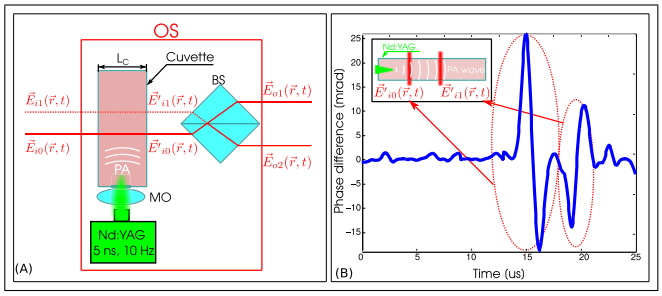

Fig. 7. (A) OS operating in the single-carrier mode. (B) Single-shot photoacoustic signal: instantaneous phase difference $\Delta\phi(n)$ between the $\vec{E}'_{i0}(\vec{r},t)$ and $\vec{E}'_{i1}(\vec{r},t)$ beams recovered by the algorithm in the PC from Eq. (14).

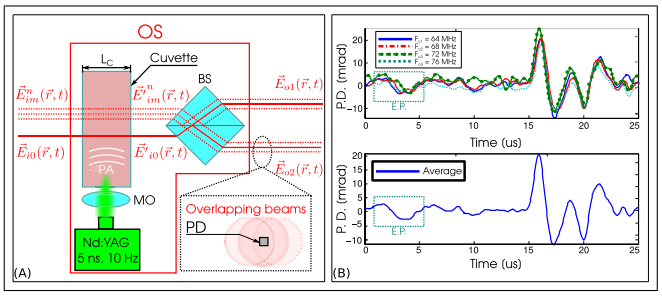

Fig. 8. (A) OS operating in the multicarrier mode. PD: Photodiode. The inset shows the overlapping of the beams at the active area of a photodiode in the O/E block. (B) Single-shot photoacoustic signals detected by the carriers (upper panel) and their average (lower panel). E.P: External perturbation. P.D.: Phase difference. The RMS noise is smaller than the lines thickness.

Therefore, setting $I_{BB} = -Q_{BB} = A$, the modulation signal from Eq. (7) is

$$m(t) = \sum_{n=1}^{N} A\cos[(\omega_0 + \omega_n)t] \tag{16}$$

This modulation signal produces a set of N First Order Comb Beams (FOCBs) into the E/O block. The modulated free beams $\vec{E}^n_{im}(\vec{r},t)$ (with $n = 1..N$) are separated in space and travel parallelly to the unmodulated beam $\vec{E}_{i0}(\vec{r},t)$. The separation between the modulated beams is related to their relative optical frequency shifts ω_n. Once the beams traverse the OS, their phases are modulated by $\Delta\phi_n(t)$. Therefore, the frequency shift ω_n between the carriers must be large enough to avoid the overlapping between the sidebands of each phase modulated carrier. Assuming that the modulation index is low, the frequencies of the carriers must be separated by at least twice the maximum frequency component of $\Delta\phi_n(t)$ [1], [22]. We also assume that there is enough spatial overlap between the output beams to ensure that the interferograms are detected by the O/E block. Under this assumption, the output signal from the O/E block within the frequency band of interest (around ω_0) may be written as,

$$v(t) = \sum_{n=1}^{N} B_n(t)\cos[(\omega_0 + \omega_n)t + \Delta\phi_n(t)] \tag{17}$$

Thus, we can recover the phase information with a single Fourier transform [28], [29], extracting the phase of each ω_n component within the specified bandwidth. In this application, the diameter of the modulated free beams is large enough for them to overlap when traversing the control volume. The output signal of the O/E block senses the overlapping region and the phase information $\Delta\phi_n(t)$ is the same for all the components of the interferometric signal (i.e. $\Delta\phi_n(t) = \Delta\phi(t)$). In this application, a four component multicarrier signal is synthesized around the central carrier frequency $\omega_0 = 2\pi$ 70 MHz. According to the expected bandwidth of $\Delta\phi(t)$ (i.e. 2 MHz), the separation between the carrier frequencies is 4 MHz. Therefore, the carrier frequencies in $m(t)$ are located in 64 MHz, 68 MHz, 72 MHz and 76 MHz respectively. The interferograms produced from the combination of the $\vec{E}'^{\,n}_{im}(\vec{r},t)$ and $\vec{E}'_{i0}(\vec{r},t)$ beams, overlap over the photodiodes in the O/E block, as described in Fig. 8(A). It can be seen from Fig. 8(B), that the instantaneous phases recovered from the carriers agree very well with each other and with the results from the single carrier technique in Fig. 7(B). Since the recovered phase information from each carrier is the same, we average the four measurements (Fig. 7(B), lower panel) to improve the signal to noise ratio (SNR) in approximately 7 dB (6 dB due to averaging plus approximately 1 dB to the reduction of 1/f noise around ω_0), as explained below.

C. Results and Discussion

The plot in Fig.7(B) shows the instantaneous phase difference, between both beams of the SDOI in the single carrier operation mode, originated by a PA wave. The interaction with each beam can be clearly seen in the figure. As it follows from Eqs.(9) and (10), the response from the interaction with $\vec{E}_{i1}(\vec{r},t)$ is attenuated and inverted with respect to the response from $\vec{E}_{i0}(\vec{r},t)$. The time delay between both responses is approximately 4.5 μs. This is consistent with the speed of sound in the medium (approximately 1500 m/s) and the geometrical distance between the beams. The time span shown Fig.7(B) is limited to only include the initial responses of the two beams to the PA wave, before any acoustic reflections. For longer time spans, multiple reflections in the cuvette appear. Our results agree very well with those reported in similar works [24], [30]–[36]. To estimate the noise floor of the measurement, we analyze the histogram of the detected phase without any PA excitation in the control volume. The histogram corresponds to a Gaussian-type distribution of zero mean. From its fitted standard deviation, the estimated noise floor of the single-carrier, single shot measurement is 0.6 mrad (RMS). This must be compared with the peak values of the first and second PA responses, approximately 25 and 10 mrad, respectively.

In the multicarrier operation mode, it can be seen that the features in the response from each carrier are analogous to that from the single carrier mode (cf. Fig. 7(B) and Fig. 8(B) (upper panel)). As described above, the time span is limited to exclude the acoustic reflections in the cuvette. The average of the responses from the four carriers (Fig.8(B) (lower panel)) agrees well with the response of each individual carrier and with the response from the single carrier mode, with an improved SNR. The noise floor of the multicarrier, single-shot measurement is 0.2 mrad (RMS). This value was obtained by means of a statistical analysis analogous to that used in

TABLE I

COMPARISON OF OUR RESULTS WITH OTHER FREE-SPACE INTERFEROMETRIC DETECTION SCHEMES. BW: BANDWIDTH, EPND: EQUIVALENT PRESSURE NOISE DENSITY, SC: SINGLE CARRIER, MC: MULTI-CARRIER. FOR LINE DETECTORS THE EPND IS NORMALIZED BY THE LENGTH OF THE DETECTOR

Reference	Detector Geometry	BW - EPND
[36]	Point	30 MHz - 3.7 Pa/$\sqrt{Hz}$
[35]	Point	1.2 MHz - 0.74 Pa/$\sqrt{Hz}$
[24]	Line	17 MHz - 0.025 Pa.mm/$\sqrt{Hz}$
This work	Line	2 MHz - 0.32 Pa.mm/$\sqrt{Hz}$ (SC) 2 MHz - 0.11 Pa.mm/$\sqrt{Hz}$ (MC)

the single-carrier mode. We checked that the histogram also corresponds to a Gaussian-type distribution of zero mean. The improvement in the SNR is due to the averaging of the phase measurement from each of the carriers, while at the same time, we also reduce the contribution of the 1/f noise of the electronic circuits. Fig. 8(B) also shows the response of the SDOI to an external mechanical perturbation (indicated as E.P. in the figure). It must be stressed that the E.P feature can be clearly identified in the averaged signal. This follows from the fact that the E.P feature has the same shape and appears simultaneously in the response from the four carriers. This is an additional advantage of the multicarrier operation mode (frequency diversity [1]), since it is very unlikely that an electrical perturbation could have simultaneously the same effect on the four carriers.

Since we can easily choose, by software selection, between both SDOI operation modes, a brief comparison between them is interesting. The main advantage of single carrier detection is that the modulation and demodulation algorithms are very straightforward, as detailed in Sec.IV-A. Thus, the software implementation of the digital processing of the detected signal $v(t)$ is very simple, since it only requires a single arithmetic operation (Eq. 14). However, since the demodulation occurs at baseband, the contribution of the 1/f noise in the electronic system degrades the SNR of the demodulated signal. This is a well-known characteristic of direct conversion receivers [1], [22]. An improvement in the SNR, by avoiding the 1/f noise, can be achieved by implementing a double conversion in the receiver, as reported in previous works [10], [11].

In the multicarrier operation mode, the modulation signal $m(t)$ is more complex. However, it is readily synthesized in the SDH without any hardware modifications, thus avoiding the additional cost and complexity of the RF hardware implementation. The added complexity in the demodulation of the received signal $v(t)$ is also easily handled by the SDH in our implementation, without any additional hardware. In summary, with this SDH implementation, the advantages of the multicarrier mode far outweigh the greater software complexity.

Table I summarizes some of the results obtained with different experimental setups. We analyze different free-space interferometers: Mach-Zehnder (MZI) [24], [35], Fabry-Perot (FPI) [36], with different detection geometries (line and point) and also different photodetection schemes. Therefore, different bandwidths (BW) and noise equivalent pressures (NEP) were achieved. In general, the time-domain response to ultrasonic point sources is similar and agrees well with those from theoretical models [30], [34]. In Table I, the NEP is normalized by the square root of the BW. That is, the value given is the equivalent pressure noise density (EPND). For line detector geometries, the EPND value is normalized by the line length. Depending on the sensing application each interferometer has different advantages. In the first place, the FPI with point detector geometry [36] has a large BW and a relatively high EPND. Second, the results reported in [35] correspond to a commercial heterodyne MZI (Polytec RSV 150) that has low BW and relatively high EPND. There is a fair agreement between the time-domain signal described in that work and those presented in the other papers indicated in Table I. Third, the MZI with line geometry detector described by Paltauf *et al.* [24] has the largest BW and lowest EPND. Finally, both operating modes (single-carrier and multi-carrier) of our heterodyne SDOI with line detection geometry has BW and EPND values comparable to those previously mentioned. Our system allows us to perform one shot measurements and, since the CV is traversed by means of multiple sensing beams a PA wave can be observed at different times and locations. Moreover, this SDOI relies in low cost components and can be easily miniaturized.

V. CONCLUSIONS

We propose a general architecture for the design of Software-Defined Optoelectronic (SDO) systems. We consider three conceptual domains: optical, analog electrical and digital electrical. The constitutive elements of the domains are the functional blocks. The electrical-optical (E/O) and Optical-Electrical (O/E) blocks translate the analog signals from the Software-Defined Hardware (SDH) into the input and output fields of the Optical System (OS), respectively. The Programmable Controller (PC) manages the SDH, interfaces the system to the outside world and defines the functionality of the optoelectronic system through a software platform.

As an implementation example, we develop a Software-Defined Optical Interferometer (SDOI). The system was implemented using a laptop computer as the PC, a commercial Software-Defined Radio (SDR) platform for the SDH, an E/O block based on an Acousto-Optic Modulator (AOM), a balanced-path, single-element interferometer as the OS and a balanced photodetector in the O/E.

The SDOI is successfully applied to the detection of laser induced photoacoustic signals in a concentrated dye solution. We exploit the flexibility of the SDO concept to implement two different operation modes in the SDOI: single carrier and multicarrier heterodyne interferometry. In the latter, we show that such space and frequency diversity improves single-shot interferometric measurements. We wish to emphasize that the SDO concept allows the SDOI described in this work to switch in real time between the single-carrier and multi-carrier operation modes, by software control only. The multicarrier modulation does not only improve the noise floor, but it also makes possible to discriminate between an external mechanical disturbance and electrical noise.

From the point of view of optoelectronic measurement systems design, most previous efforts have been directed to improve the performance through the optimization of the processing of the received signal, according to the paradigm of Wiener [37]. Following the concepts developed initially by Shannon [38], the flexibility afforded by the SDO architecture makes it possible to optimize both the transmitted waveform and the processing of the received signal. This clearly broadens the possibilities for the optimization of optoelectronic systems.

REFERENCES

[1] B. P. Lathi, *Modern Digital and Analog Communication Systems 3e Osece*. Oxford, U.K.: Oxford Univ. Press, 1998.

[2] S. S. Haykin, M. Moher, and T. Song, *An Introduction to Analog and Digital Communications*, vol. 1. New York, NY, USA: Wiley, 1989.

[3] *Arduino*. Accessed: Feb. 2018. [Online]. Available: https://www.arduino.cc/en/Guide/Introduction

[4] *Red Pitaya*. Accessed: Feb. 2018. [Online]. Available: https://www.redpitaya.com/

[5] Lime Microsystems. *LMS7002M-FPRF MIMO Transceiver IC With Integrated Microcontroller*. Accessed: Feb. 2018. [Online]. Available: http://www.limemicro.com/products/software-defined-radio/

[6] Ettus Research. *USRP B200mini Series*. Accessed: Feb. 2018. [Online]. Available: https://www.ettus.com/product/details/USRP-B200mini

[7] T. J. Rouphael, *RF and Digital Signal Processing for Software-Defined Radio*. Guildford, U.K.: LimeMicrosystems, 2009.

[8] F. Scotti, F. Laghezza, P. Ghelfi, and A. Bogoni, "Multi-band software-defined coherent radar based on a single photonic transceiver," *IEEE Trans. Microw. Theory Techn.*, vol. 63, no. 2, pp. 546–552, Feb. 2015.

[9] M. Čížek, V. Hucl, J. Hrabina, R. Šmíd, B. Mikel, J. Lazar, and O. Čí, "Two-stage system based on a software-defined radio for stabilizing of optical frequency combs in long-term experiments," *Sensors*, vol. 14, no. 1, pp. 1757–1770, 2014.

[10] L. M. Riobó, F. E. Veiras, M. T. Garea, and P. A. Sorichetti, "Applications of software defined radio to heterodyne optoelectronics," in *Proc. Frontiers Opt. Soc. Amer. (OSA)*, 2017, paper JTu2A.23.

[11] L. M. Riobo, F. E. Veiras, M. G. Gonzalez, M. T. Garea, and P. A. Sorichetti, "High-speed real-time heterodyne interferometry using software-defined radio," *Appl. Opt.*, vol. 57, no. 2, pp. 217–224, Jan. 2018.

[12] *Lime Microsystems*. Accessed: Feb. 2018. [Online]. Available: https://myriadrf.org/projects/limesdr/

[13] S. Yoon, Y. Park, and K. Cho, "A new balanced-path heterodyne I/Q-interferometer scheme for low environmental noise, high sensitivity phase measurements for both reflection and transmission geometry," *Opt. Express*, vol. 21, no. 18, p. 20722–20729, Sep. 2013.

[14] J. A. Ferrari and E. M. Frins, "Single-element interferometer," *Opt. Commun.*, vol. 279, no. 2, pp. 235–239, 2007.

[15] J. D. Ellis, *Field Guide to Displacement Measuring Interferometry*. Bellingham, WA, USA: SPIE, 2014.

[16] C. E. M. Strauss, "Synthetic-array heterodyne detection: A single-element detector acts as an array," *Opt. Lett.*, vol. 19, no. 20, pp. 1609–1611, Oct. 1994.

[17] C. Scruby and L. Drain, *Laser Ultrasonics Techniques and Applications*. New York, NY, USA: Taylor & Francis, 1990.

[18] J. Graeme, *Photodiode Amplifiers: OP AMP Solutions* (Gain Technology). New York, NY, USA: McGraw-Hill, 1996.

[19] OSRAM. *SFH 2701 High Speed Pin Photodiode*. Accessed: Feb. 2018. [Online]. Available: https://www.osram.com

[20] Texas Instruments. *OPA657 1.6-GHz, Low-Noise, FET-Input Operational Amplifier*. Accessed: Feb. 2018. [Online]. Available: http://www.ti.com/lit/ds/symlink/opa657.pdf

[21] L. M. Riobo, F. E. Veiras, P. A. Sorichetti, and M. T. Garea, "Wideband transimpedance amplifiers for optoelectronics: Applications to dynamic interferometry," *Revista Elektron*, vol. 1, no. 1, pp. 16–19, Jul. 2017.

[22] J. B. Tsui, *Digital Techniques for Wideband Receivers*, vol. 2. Rijeka, Croatia: SciTech, 2004.

[23] GNU Project. *GNU Radio*. Accessed: Feb. 2018. [Online]. Available: https://www.gnuradio.org

[24] G. Paltauf, R. Nuster, M. Haltmeier, and P. Burgholzer, "Photoacoustic tomography using a Mach–Zehnder interferometer as an acoustic line detector," *Appl. Opt.*, vol. 46, no. 16, pp. 3352–3358, 2007.

[25] S. M. Maswadi *et al.*, "All-optical optoacoustic microscopy based on probe beam deflection technique," *Photoacoustics*, vol. 4, no. 3, pp. 91–101, 2016.

[26] A. Hochreiner, J. Bauer-Marschallinger, P. Burgholzer, B. Jakoby, and T. Berer, "Non-contact photoacoustic imaging using a fiber based interferometer with optical amplification," *Biomed. Opt. Express*, vol. 4, no. 11, pp. 2322–2331, Nov. 2013.

[27] J. Bauer-Marschallinger, K. Felbermayer, and T. Berer, "All-optical photoacoustic projection imaging," *Biomed. Opt. Express*, vol. 8, no. 9, pp. 3938–3951, Sep. 2017.

[28] R. van Nee and R. Prasad, *OFDM for Wireless Multimedia Communications*. Norwood, MA, USA: Artech House, 2000.

[29] M. Takeda, H. Ina, and S. Kobayashi, "Fourier-transform method of fringe-pattern analysis for computer-based topography and interferometry," *J. Opt. Soc. Amer. A, Opt. Image Sci.*, vol. 72, no. 1, pp. 156–160, 1982.

[30] I. G. Calasso, W. Craig, and G. J. Diebold, "Photoacoustic point source," *Phys. Rev. Lett.*, vol. 86, no. 16, p. 3550, 2001.

[31] M. G. González, "Determination of the photoluminescence quantum yield of diluted dye solutions in highly scattering media by pulsed photoacoustic spectroscopy," *Appl. Opt.*, vol. 49, no. 36, pp. 6850–6854, 2010.

[32] K. Quan, H. A. MacKenzie, P. Hodgson, and G. B. Christison, "Photoacoustic generation in liquids with low optical absorption," *Ultrasonics*, vol. 32, no. 3, pp. 181–186, 1994.

[33] T. Schmid, U. Panne, R. Niessner, and C. Haisch, "Optical absorbance measurements of opaque liquids by pulsed laser photoacoustic spectroscopy," *Anal. Chem.*, vol. 81, no. 6, pp. 2403–2409, 2009.

[34] A. C. Tam, "Applications of photoacoustic sensing techniques," *Rev. Modern Phys.*, vol. 58, no. 2, p. 381, 1986.

[35] C. Tian *et al.*, "Non-contact photoacoustic imaging using a commercial heterodyne interferometer," *IEEE Sensors J.*, vol. 16, no. 23, pp. 8381–8388, Dec. 2016.

[36] P. C. Beard, F. Perennes, and T. N. Mills, "Transduction mechanisms of the Fabry-Perot polymer film sensing concept for wideband ultrasound detection," *IEEE Trans. Ultrason., Ferroelectr., Freq. Control*, vol. 46, no. 6, pp. 1575–1582, Nov. 1999.

[37] N. Wiener, *Extrapolation, Interpolation, and Smoothing of Stationary Time Series*. Cambridge, MA, USA: MIT Press, 1964.

[38] C. E. Shannon, "A mathematical theory of communication," *Bell Syst. Tech. J.*, vol. 27, no. 3, pp. 379–423, Jul./Oct. 1948.

Lucas M. Riobó (M'16) received the Engineering degree in electronics engineering from the Universidad de Buenos Aires, Argentina, in 2014. He is currently pursuing the Ph.D. degree, with a doctoral scholarship, from the National Scientific and Technical Research Council. He is also with the Group of Laser, Optical Materials and Electromagnetic Applications as a Research Member. His current research interests include optoelectronics design and signal processing and dynamic interferometry.

Francisco E. Veiras (M'16) received the Doctor Engineering (Ph.D.) degree in electronics engineering in 2008 and received the Ph.D. *(summa cum laude)* degree from the Universidad de Buenos Aires (UBA), Argentina, in 2013. He is currently a Teaching Assistant and a Researcher at UBA and CONICET. His current projects are centered around the research and development of polarization control devices and crystal optics, interferometry, optical techniques for inspection and detection in micro and nanosystems, nondestructive testing, and ultrasonic biomedical imaging. He is a member of SPIE and OSA.

María T. Garea (M'16) received the Doctor (Ph.D.) degree in physics in 1985 and received the Ph.D. degree from the Universidad de Buenos Aires in 1993. She is currently a full-time Associate Professor and a Coordinator of the Optical Applications Laboratory. Her current work includes materials optics, polarization, optical devices, interferometry, and physics teaching.

Patricio A. Sorichetti (S'85–M'91–SM'00) graduated in physics *(cum laude)* and in electronics engineering from the Universidad de Buenos Aires (UBA), in 1990 and 1991, respectively, and received the Ph.D. *(suma cum laude)* degree from UBA in 2012. He is currently an Associate Professor with the Physics Department, School of Engineering, UBA. His current research interests include the mechanical and electrical properties of polymers and complex fluids. He is a member of the IEEE Photonics Society. He was the President of the Argentine Section of the Communications Society of the IEEE from 2001 to 2002.